

Article

## Nanomechanical Properties and Deformation Behaviors of Multi-Component (AlCrTaTiZr) $N_xSi_y$ High-Entropy Coatings

Shao-Yi Lin, Shou-Yi Chang \*, Chia-Jung Chang and Yi-Chung Huang

Department of Materials Science and Engineering, National Chung Hsing University, Taichung 40227, Taiwan; E-Mails: ck910435@yahoo.com.tw (S.-Y.L.); cjchang1096@yahoo.com.tw (C.J.C.); u8907010@yahoo.com.tw (Y.-C.H.)

\* Author to whom correspondence should be addressed; E-Mail: shouyi@dragon.nchu.edu.tw; Tel.: +886-4-22857517; Fax: +886-4-22857017.

Received: 27 September 2013; in revised form: 20 November 2013 / Accepted: 18 December 2013 / Published: 31 December 2013

---

**Abstract:** In this study multi-component (AlCrTaTiZr) $N_xSi_y$  high-entropy coatings were developed by co-sputtering of AlCrTaTiZr alloy and Si in an Ar/N<sub>2</sub> mixed atmosphere with the application of different substrate biases and Si-target powers. Their nanomechanical properties and deformation behaviors were characterized by nanoindentation tests. Because of the effect of high mixing entropies, all the deposited multi-component (AlCrTaTiZr) $N_xSi_y$  high-entropy coatings exhibited a simple face-centered cubic solid-solution structure. With an increased substrate bias and Si-target power, their microstructures changed from large columns with a [111] preferred orientation to a nanocomposite form with ultrafine grains. The hardness, H/E ratio and H<sup>3</sup>/E<sup>2</sup> ratio of (AlCrTaTiZr) $N_{1.07}Si_{0.15}$  coating reached 30.2 GPa, 0.12 and 0.41 GPa, respectively, suggesting markedly suppressed dislocation activities and a very high resistance to wear and plastic deformation, attributable to grain refinements and film densification by the application of substrate bias, a nanocomposite structure by the introduction of silicon nitrides, and a strengthening effect induced by severe lattice distortions. In the deformed regions under indents, stacking faults or partial dislocations were formed, while in the stress-released regions, near-perfect lattices recovered.

**Keywords:** multi-component; high-entropy alloy; nanomechanical property; deformation

---

## 1. Introduction

Protective hard coatings with good mechanical properties, high thermal stabilities, and also a high resistance to wear and corrosion have been widely developed for improving the lifetime of machinery tool components [1]. Because of the strict demands for practical applications under ever larger mechanical stresses and higher temperatures, more robust coatings have been investigated to replace conventional single-layered, single-phase, unitary metals or metallic compounds (such as TiN, CrN, TiC, *etc.*), by introducing stacked structures (TiN/TiC, TiC/VC, TiCN/ZrCN [2–4]), nanocomposite structures (nc-TiN/a-Si<sub>3</sub>N<sub>4</sub>, nc-TiN/a-BN, nc-TiN/a-Si<sub>3</sub>N<sub>4</sub>/TiSi<sub>2</sub>, where nc = nanocrystalline, a = amorphous [5,6]), and/or multiple components (ternary CrZrN, ZrCN, CrCN, TiCN [7–10], and quaternary TiAlCN, TiSiCN [11,12]), as well as forming stacked, multi-component nanocomposite structures (TiAlN/TiN/Al<sub>2</sub>O<sub>3</sub> [13]) with good mechanical performance. In recent years, Yeh developed a new alloy system, named “high-entropy alloy” (HEA), which is composed of five or more metallic elements in an equimolar or near-equimolar ratio [14]. Multi-component HEAs typically possess very simple solid-solution structures because of the effect of high mixing entropies to lower free energy [14], and exhibit extraordinary performances such as good mechanical properties, high thermal stabilities, and an excellent wear resistance [14–16]. Accordingly, HEAs, HEA nitrides (HEANs), HEA carbides (HEACs) and HEA carbonitrides (HEACNs) have been intensively studied for protective coating applications [17–21].

The addition of Si improves the mechanical properties and oxidation resistance of hard metal nitride coatings; ex. the formation of amorphous SiN<sub>x</sub> regions at the grain boundaries of TiN inhibits the growth of TiN nanograins and suppresses the penetration of oxygen through the grain boundaries [22,23]. A minor addition of Si to form a nc-TiN/a-Si<sub>3</sub>N<sub>4</sub> nanocomposite structure provided a high hardness up to 38 GPa; however, an excess Si content led to the thickening of the surrounding amorphous Si<sub>3</sub>N<sub>4</sub> layers and a reduction in hardness [24]. The Ti-Si-N system presented better thermal stabilities than Ti-Al-N did [25–27], and all other Si-doped systems, including Zr-Si-N, Al-Si-N and Cr-Si-N, also showed a hardness higher than 35 GPa [28–31]. Because of the anticipated improvement in mechanical performance by the severe lattice distortions of multi-component HEAs with different atom sizes [17,19,21], the strong covalent bonds of incorporated Si [22], the grain refinements and strengthening by amorphous SiN<sub>x</sub> boundary layers [22,23], and also the large lattice mismatches between nitrides and silicides (similar to those between nitrides and carbides [21]), multi-component (AlCrTaTiZr)N<sub>x</sub>Si<sub>y</sub> high-entropy coatings (denoted as HEAN<sub>x</sub>Si<sub>y</sub>, x and y: N- and Si-to-HEA content ratios) were thus developed in this study by co-sputtering of AlCrTaTiZr alloy and Si in an Ar/N<sub>2</sub> mixed atmosphere, and their mechanical properties and deformation behaviors on the nanoscale were characterized.

## 2. Experimental Section

Multi-component HEAN<sub>x</sub>Si<sub>y</sub> coatings with a thickness of about 700–800 nm were deposited on Si substrates by reactive magnetron co-sputtering of AlCrTaTiZr HEA and Si targets in an Ar/N<sub>2</sub> mixed atmosphere. The HEA target was prepared with an equimolar quinary alloy (components: Al, Cr, Ta, Ti, Zr) by vacuum arc-melting the constituent elements uniformly, followed by cutting and polishing

of the solidified bulk to a disc of 50 mm in diameter. Depositions were performed at room temperature, an HEA-target power of 150 W (radio-frequency) and different Si-target powers (0, 25, 50, 100, 200 W; direct current) with the application of different substrate biases (0,  $-100$  or  $-150$  V). The total gas flow (Ar+N<sub>2</sub>) rate was controlled at 30 sccm (a working pressure of 0.8 Pa), and the N<sub>2</sub>-to-total flow ratio was adjusted as 10%. A scanning electron microscope (SEM, JEOL JSM-6700F) was used to observe the surface morphologies and cross-sectional microstructures of the HEAN<sub>x</sub>Si<sub>y</sub> coatings. Elemental compositions were determined by energy dispersive spectrometry (EDS, Oxford Inca Energy 400) and field-emission electron probe microanalyses (FE-EPMA, JEOL JXA-8800M). The crystal structures were analyzed by a glancing incident angle X-ray diffractometer (GIAXRD, Rigaku Dmax 2000). The microstructures and lattice images of the coatings were examined by a high-resolution transmission electron microscope (TEM, JEOL JEM-2100F). The hardness and elastic modulus were measured using a TriboLab nanoindenter (Hysitron) with a Berkovich indenter (tip radius 50 nm, edge angle 130.6°) at a maximum load of 2,000 μN under a loading/unloading rate of 200 μN/s, in an ambient atmosphere, by using an Oliver-Pharr method. The indentation depths were controlled at below 1/10 of film thickness to avoid any substrate effect [32,33]; before the tests, the contact area function of the indenter tip was precisely calibrated. Five to ten tests were carried out for each sample. To examine the deformation behaviors of the coatings, a UMIS nanoindenter (Base Model, CSIRO) with a Berkovich indenter (tip radius 150 nm) was applied to indent the coatings at a large load of 400 mN. The cross-sectional microstructures and lattice structures of the deformed regions under indent marks and the undeformed regions far away from the indents were examined by a high-resolution TEM. The thin foils for TEM observations were cut from the coatings, with a top Pt protection layer, by a focused ion beam (FIB, FEI Nova 200) at a low current down to 50 pA.

### 3. Results and Discussion

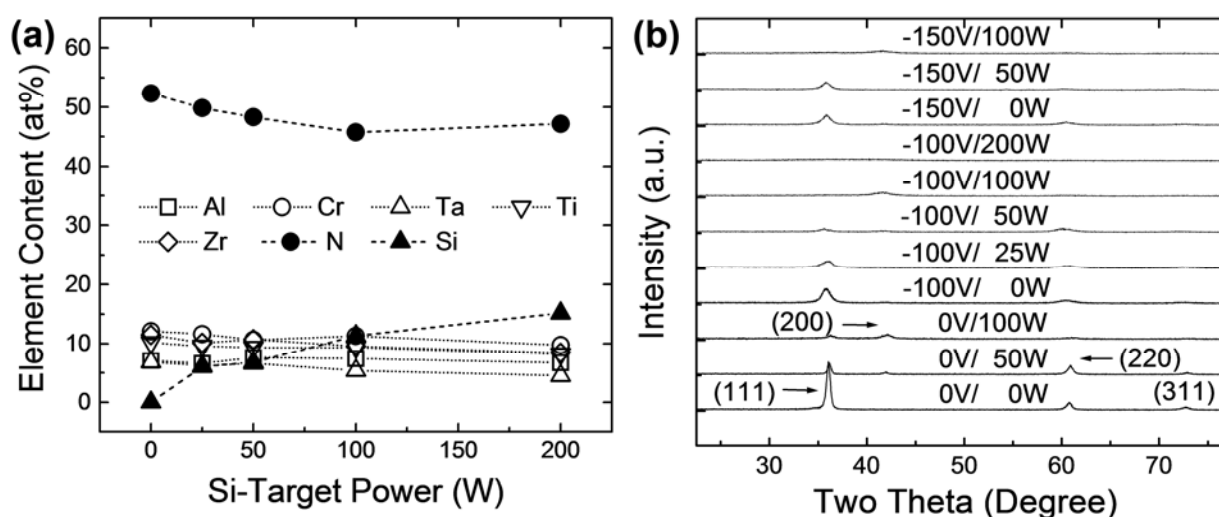
#### 3.1. Compositions and Structures of HEAN<sub>x</sub>Si<sub>y</sub> Coatings

Figure 1(a) shows the elemental compositions of HEAN<sub>x</sub>Si<sub>y</sub> coatings deposited at a substrate bias of  $-100$  V and different Si-target powers. Very close to the designed compositions, the HEAN<sub>x</sub> coating ( $x \sim 1.10$ , *i.e.*, HEA:N:Si  $\sim 1:1.10:0$ , as listed in Table 1), without applying Si-target power, consisted of 52 at% N and near-equimolar metallic elements (each about 9.5 at%). Minor excess N was expected to exist, interstitially, in the lattices of the metal nitride structure. As the Si-target power increased to 200 W, Si was obviously doped in the HEAN<sub>x</sub>Si<sub>y</sub> coatings, and its content accordingly increased to 15 at%, while the N content decreased to 46–47 at% and remained at the same level. All the contents of metallic elements decreased as well, but however their near-equimolar ratio remained. At a Si-target power of 50 W, the HEA:N:Si ratio of about 1:1.07:0.15 indicated that most of the doped Si might possibly bond the excess interstitial N to form strong covalent SiN-based compounds because of their high formation enthalpies (for example, Si<sub>3</sub>N<sub>4</sub>  $-742$  kJ/mol [34]). However, at a high power up to 100–200 W, much more excess Si ( $y \sim 0.26$ – $0.40$ ) was doped and expected to react with the metallic elements and form metal silicides besides more SiN-based compounds.

Figure 1(b) plots the XRD patterns of HEAN<sub>x</sub>Si<sub>y</sub> coatings deposited at different substrate biases and Si-target powers. It was interestingly found that even with different deposition parameters, all the

obtained HEAN<sub>x</sub>Si<sub>y</sub> coatings have only one set of diffraction peaks at about 35.6°, 42.1°, 60.9°, and 72.6°. According to the Bragg law and the relation between interplanar spacing *d* and (*hkl*) lattice [35], these peaks corresponded to the (111), (200), (220), (311) lattices of the NaCl-type face-centered cubic (fcc) structure. This finding clearly indicated that due to the effect of high mixing entropies of multiple components, the HEAN<sub>x</sub>Si<sub>y</sub> coatings formed a simple solid-solution structure, rather than any complex phase separations [17–21], in which five metallic elements randomly distributed at the “Na” site of the NaCl-type fcc structure, while N located at the “Cl” site [26,36,37]. As listed in Table 1, without Si doping, the interplanar spacing of HEAN<sub>x</sub> (111) lattice was 0.251 nm approximate to the average spacing of five metal nitrides (AlN, CrN, TaN, TiN, ZrN) [19,21]. With increasing Si-target power, the (111) interplanar spacing did not obviously change because the doped Si was believed to bond the excess interstitial N to form amorphous SiN-based compounds [21–23].

**Figure 1.** (a) Elemental compositions of HEAN<sub>x</sub>Si<sub>y</sub> coatings deposited at a substrate bias of −100 V and different Si-target powers. (b) XRD patterns of HEAN<sub>x</sub>Si<sub>y</sub> coatings deposited at different substrate biases and Si-target powers.



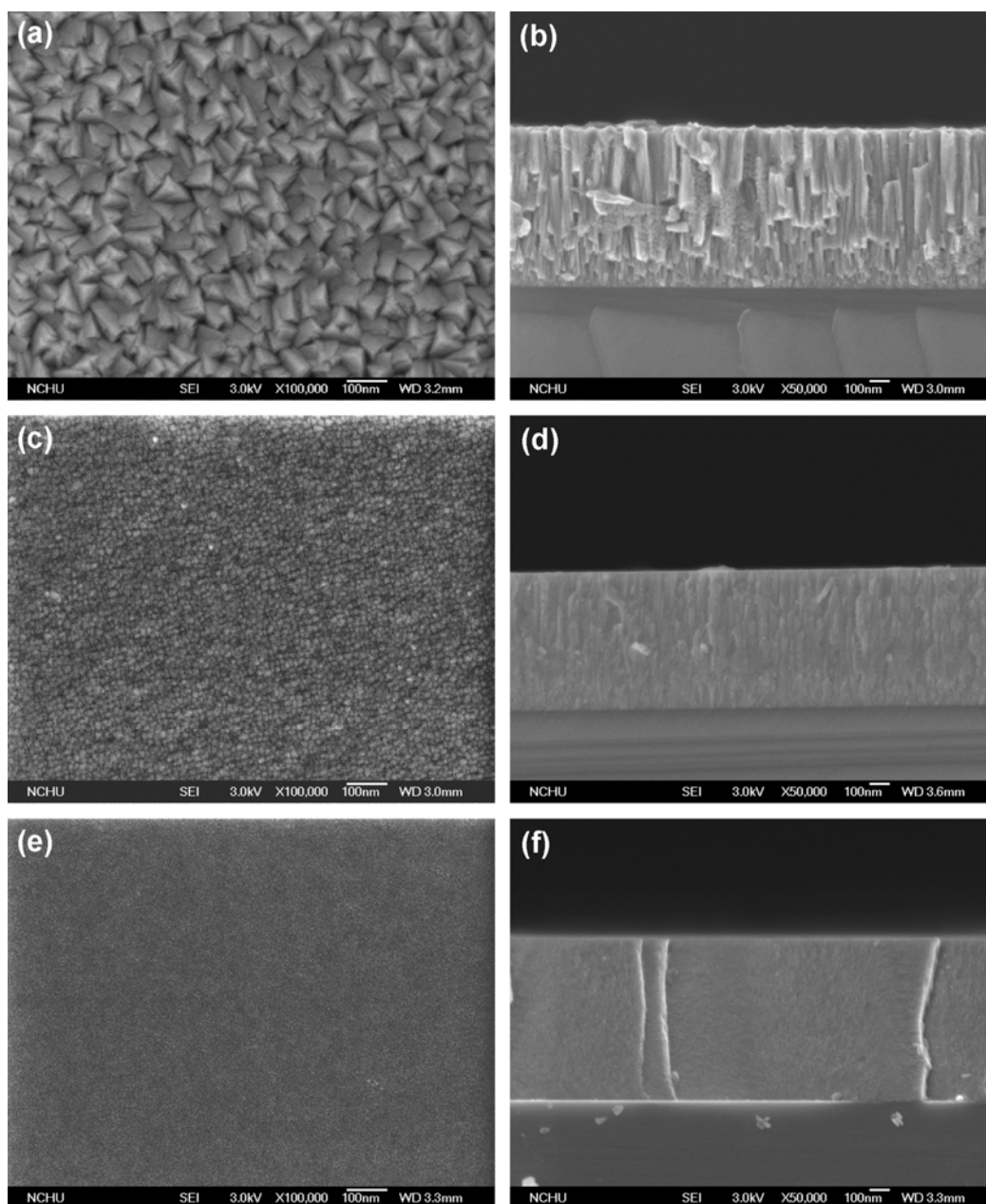
**Table 1.** HEA:N:Si content ratios, the diffraction angles ( $2\theta$ ) and interplanar spacing (*d*) of fcc (111) lattice, the full widths at half maxima (FWHM) of fcc (111) diffraction peaks, and grain sizes of HEAN<sub>x</sub>Si<sub>y</sub> coatings deposited at a substrate bias of −100 V and different Si-target powers.

Si-target power (W)	0	25	50	100	200
HEA:N:Si	1:1.10:0	1:1.13:0.14	1:1.07:0.15	1:1.06:0.26	1:1.25:0.40
$2\theta_{111}$ (°)	35.78	35.64	35.59	35.74	-
$d_{111}$ (nm)	0.251	0.252	0.252	0.251	-
FWHM <sub>111</sub> (°)	1.04	1.08	1.116	-	-
Grain size (nm)	8	8	7	< 7	< 7

However, with increasing Si-target power, the preferred orientations and microstructures of the HEAN<sub>x</sub>Si<sub>y</sub> coatings obviously changed, as seen from the XRD patterns in Figure 1(b) and observed in the SEM surface morphologies and cross-sectional microstructures in Figure 2. At a substrate bias of 0 V and a Si-target power of 0 W, the HEAN<sub>x</sub> coating exhibited a [111] preferred growth orientation and

a large columnar structure with a pyramid-like surface (size  $\sim 50\text{--}60$  nm), as seen in Figure 2(a) and Figure 2(b). At a Si-target power above 50 W, the preferred orientations of the  $\text{HEAN}_x\text{Si}_y$  coatings then changed to [200], and the microstructures very clearly changed to ultrafine grains with a dome-like surface (size  $\sim 10$  nm) as in Figure 2(c) and Figure 2(d), possibly due to the competition between surface energy and strain energy [17,19,21], or even became amorphous-like with a very smooth surface as in Figure 2(e) and Figure 2(f).

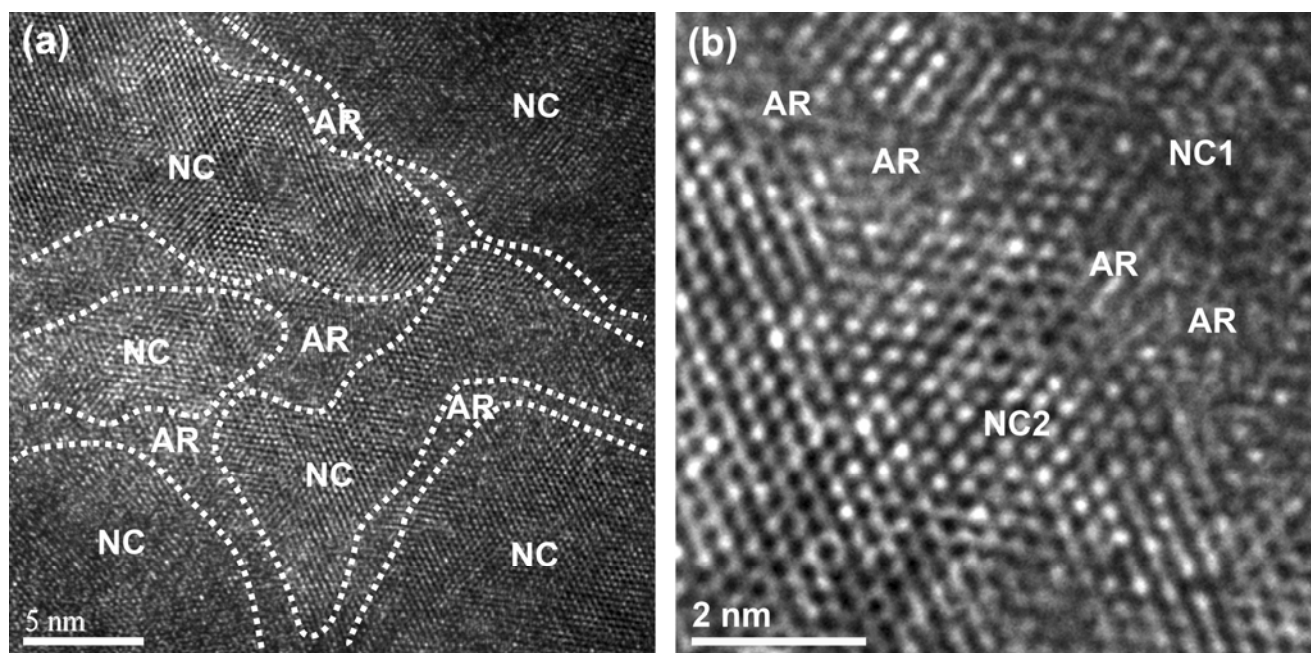
**Figure 2.** SEM surface morphologies (left) and cross-sectional microstructures (right) of  $\text{HEAN}_x\text{Si}_y$  coatings deposited at different substrate biases and Si-target powers: (a), (b) bias 0 V, power 0 W; (c), (d) bias  $-100$  V, power 50 W; (e), (f) bias  $-150$  V, power 100 W.



From the full widths at half maxima (FWHM) of the fcc (111) diffraction peaks and the Sherrer equation [35], the grain sizes of  $\text{HEAN}_x\text{Si}_y$  coatings listed in Table 1 were obtained and found to decrease to a very small level of less than 7 nm with increasing substrate bias and Si-target power,

consistent with the above SEM observations. As shown in the TEM lattice image of  $\text{HEAN}_{1.07}\text{Si}_{0.15}$  coating (deposited at a substrate bias of  $-100$  V and a Si-target power of 50 W) in Figure 3(a), ultrafine grains with a size of 5–15 nm and small-angle boundaries with a preferred orientation were clearly identified [18,21,36]. As seen in Figure 3(b), amorphous regions (ARs) were found to exist between two nanocrystallites (NC1 and NC2) of small-angle misorientation. The interplanar spacing of these nanocrystallites of about 0.253 nm consisted with the value of fcc (111) lattice of  $\text{HEAN}_x$  obtained by XRD analyses (0.251 nm), revealing a random and uniform solid-solution distribution of five metallic elements. The amorphous regions at the grain boundaries of the metal nitrides were then expected to be mainly composed of SiN-based compounds [22,23] because the interplanar spacing of  $\text{HEAN}_x\text{Si}_y$  would markedly expand if the SiN-based compounds of large lattice constants (cubic  $\text{Si}_3\text{N}_4$ , 0.7639 nm; the radius of Si atom 0.111 nm [1]) were incorporated in the  $\text{HEAN}_x$  grains. The  $\text{HEAN}_x$  nanograins and the SiN-based boundaries would form a nanocomposite structure [20,34], and the SiN-based boundaries would inhibit the growth of the nitride nanograins [22,34], as the decrease in grain size in this study. Also, a high substrate bias or Si-target power would induce strong ion bombardments and yield the densification and grain refinements of the coatings [38].

**Figure 3.** (a) TEM lattice image of  $\text{HEAN}_{1.07}\text{Si}_{0.15}$  coating deposited at a substrate bias of  $-100$  V and a Si-target power of 50 W (NC: nanocrystalline, AR: amorphous regions). (b) Magnified image of (a), showing ARs between NC1 and NC2 of small-angle misorientation.



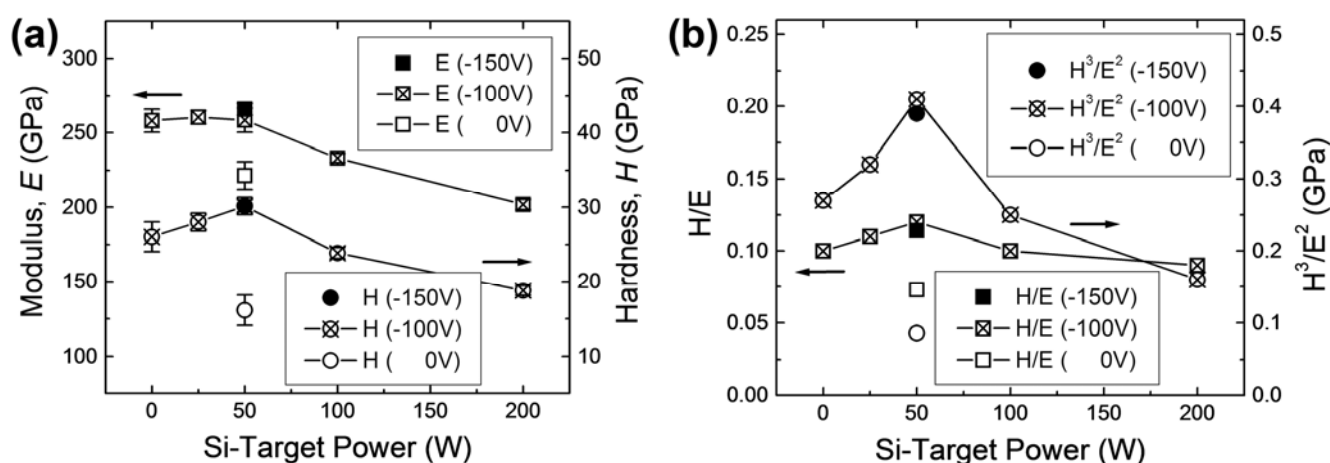
### 3.2. Mechanical Properties and Deformation Behaviors of $\text{HEAN}_x\text{Si}_y$ Coatings

Figure 4(a) shows the mechanical properties of  $\text{HEAN}_x\text{Si}_y$  coatings deposited at different substrate biases and Si-target powers. At a substrate bias of  $-100$  V, with increasing Si-target power from 0 to 50 W, the hardness increased from 26.0 GPa to the highest value 30.2 GPa, very possibly attributed to (1) the formation of strong covalent-like SiN-based compounds [10], (2) the solution strengthening by the incorporations of different-size atoms, (3) the surrounding amorphous SiN-based compounds at the

grain boundaries of metal nitrides to form a nanocomposite structure [20,32], (4) the inhibition of nitride grain growth by the surrounding amorphous SiN-based compounds for grain refinements, and (5) the strong bombardments of high Si-target power to yield film densification and grain refinements [36]. However, the modulus remained at about 258 GPa because the minor Si doping and the small amount of SiN-based compounds would not change the intrinsic elastic property. Unfortunately, at a higher Si-target power up to 100 or 200 W, the hardness decreased to 23.9 or only 18.8 GPa, and the modulus decreased to 233 or 202 GPa, due to the addition of more excess Si ( $y \sim 0.26\text{--}0.40$ ). Excess Si was expected to react with metallic elements and form brittle metal silicides, besides thick surrounding amorphous SiN-based compounds, lowering the mechanical properties of the coatings. An increased substrate bias also effectively improved the mechanical properties because of film densification and grain refinements [36], as well as large residual compressive stresses [32,38,39].

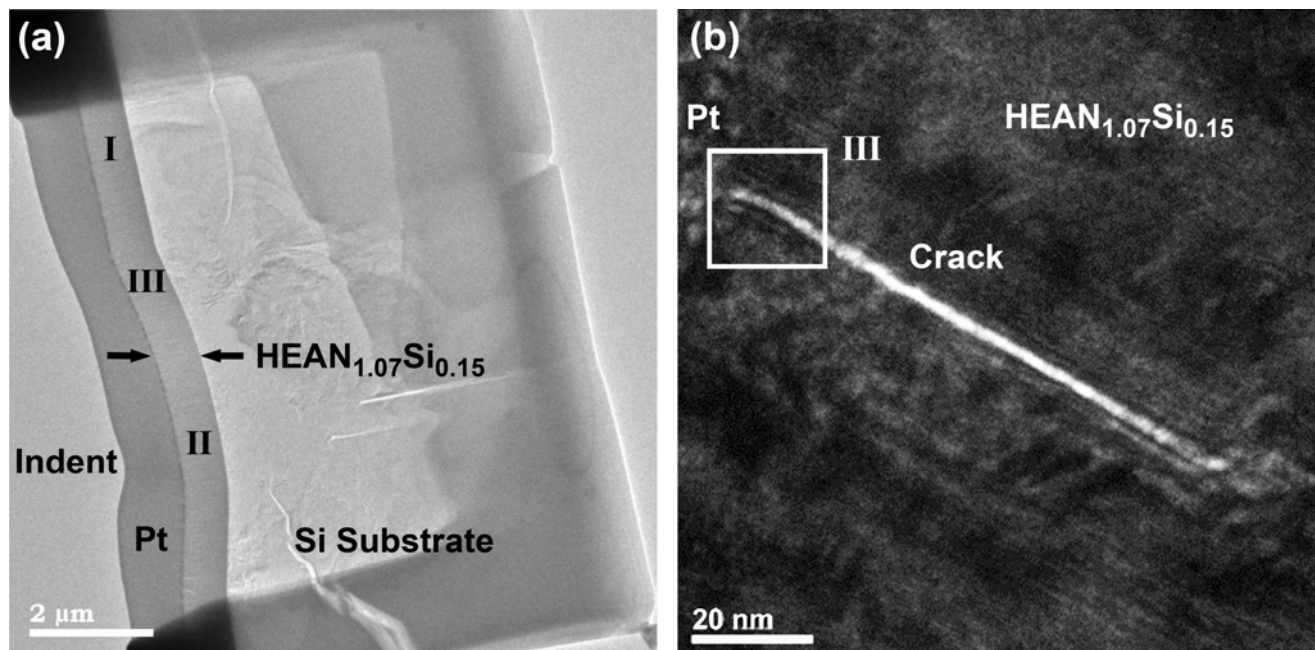
Figure 4(b) plots the  $H/E$  and  $H^3/E^2$  ratios ( $H$ : hardness,  $E$ : modulus), important prediction indices of the resistance to wear and plastic deformation [1,40], of  $\text{HEAN}_x\text{Si}_y$  coatings deposited at a substrate bias of  $-100$  V and different Si-target powers. Similar to the variation of hardness, the  $H/E$  and  $H^3/E^2$  ratios increased from 0.10 and 0.27 GPa to the highest values 0.12 and 0.41 GPa, respectively, with Si-target power from 0 to 50 W, indicating that a minor (proper) amount of Si doping to form amorphous SiN-based compounds at the boundaries of metal nitrides efficiently enhanced the wear resistance and the overall mechanical performance of the coatings. As the Si-target power further increased, the  $H/E$  and  $H^3/E^2$  ratios would then decrease to only 0.09 and 0.16 GPa, respectively, due to the formation of metal silicides and the thickening of amorphous SiN-based compounds with excess Si [24].

**Figure 4.** (a) Hardness ( $H$ ) and elastic modulus ( $E$ ) and (b)  $H/E$  and  $H^3/E^2$  ratios of  $\text{HEAN}_x\text{Si}_y$  coatings deposited at different substrate biases and Si-target powers.



The  $\text{HEAN}_{1.07}\text{Si}_{0.15}$  coating (deposited at a substrate bias of  $-100$  V and a Si-target power of 50 W) presented the best mechanical performance as well as the highest predicted wear resistance. Therefore, its nanoscale deformation behavior was examined by indenting the coating with a high load of 400 mN and FIB-cutting the sample into thin foils for TEM observations, as shown in Figure 5 (before FIB cutting, the sample was coated with a top Pt protection layer to avoid possible damage caused by ion beam bombardment).

**Figure 5.** (a) TEM image of FIB-cut foil of indented HEAN<sub>1.07</sub>Si<sub>0.15</sub> coating deposited at a substrate bias of  $-100$  V and a Si-target power of 50 W: (I) undeformed region away from an indent, (II) deformed region under an indent, (III) stress-released region around a crack. (b) Magnified image of region III (stress-released region around a crack).



Three regions were examined, including the undeformed region (I, far away from the indent mark), the deformed region (II, just under the indent), and the stress-released region (III, around a crack). As seen in the HRTEM lattice image of the undeformed region in Figure 6(a), similar to the microstructure shown in Figure 3(a), a nanocomposite structure with aligned ultrafine grains and surrounding amorphous boundaries was clearly observed. The selected area diffraction (SAD) pattern with annularly diffused spots confirmed a typical polycrystalline columnar structure with a preferred orientation [41,42]. Also, radially expanded spots were observed, which were very possibly caused by strained lattices (severe lattice distortions and partial dislocations [18,36]) as seen in the Fast Fourier Transform (FFT) image in Figure 6(b), due to the additions of five different-size metal atoms (Al, Cr, Ta, Ti, Zr). By comparison, under severe deformations, as seen in the lattice image and SAD pattern in Figure 7(a) as well as the FFT image in Figure 7(b), the radial expansion of diffraction spots became more obvious, and more severely distorted lattices were seen. This finding suggested that, under indentation, much larger stresses/strains were introduced to the lattices, and thus stacking faults and more partial dislocations were clearly formed. These stacking faults and partial dislocations, rather than complete dislocations, were found to distribute and believed to slide along the small-angle boundaries of the nano-columnar structure [18,36], dominating the deformation behaviors of the multi-component HEAN<sub>x</sub>Si<sub>y</sub> coatings with large lattice distortions and high strain energy [43]. Interestingly, at the stress-released region around a crack (near the indent mark), the lattice and FFT images in Figure 8 revealed the formation of near-perfect lattices without distortions, stacking faults or dislocations. The high strain energy that was attributed the application of high indentation stresses and the addition of different-size atoms was expected to be released during film cracking. The reversible activities (formation and disappearance) of stacking faults and partial dislocations therefore led to the recovery of the ordered and perfect lattice structure as observed.

**Figure 6.** HRTEM analyses of undeformed HEAN<sub>1.07</sub>Si<sub>0.15</sub> coating deposited at a substrate bias of  $-100$  V and a Si-target power of 50 W (region I in Figure 5, away from an indent): (a) lattice image and SAD pattern, (b) FFT image marked in (a) (solid circles: possible complete dislocations; dashed circles: possible partial dislocations).

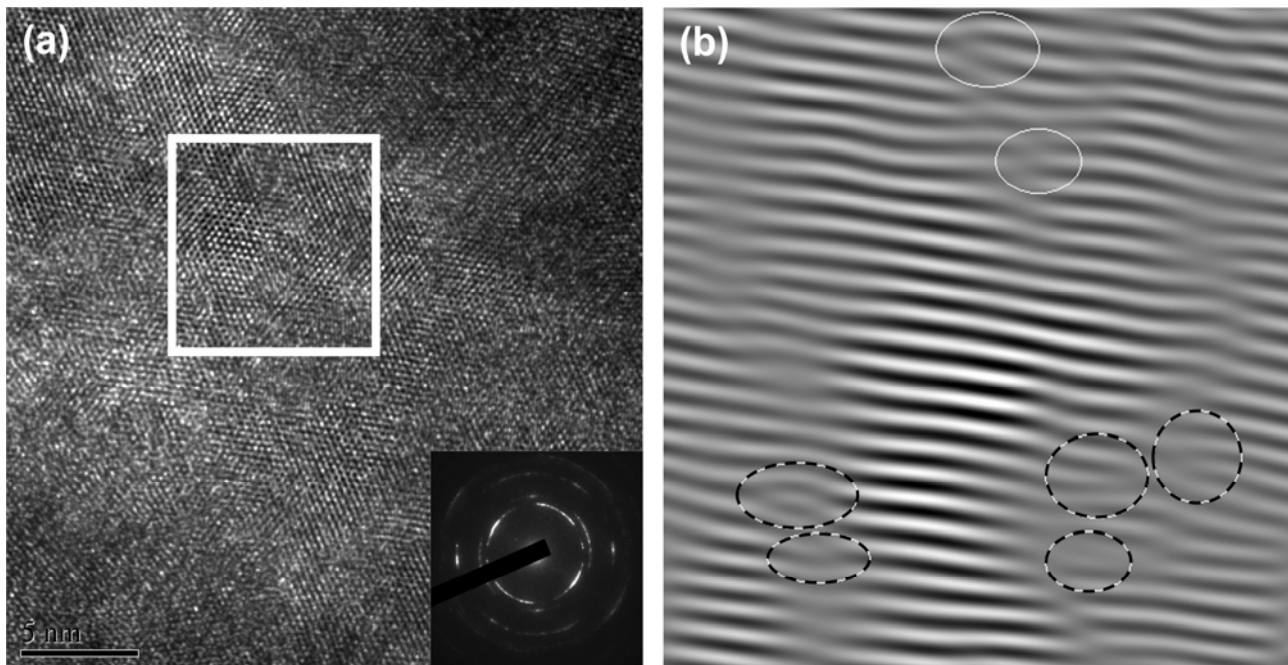


**Figure 7.** HRTEM analyses of deformed HEAN<sub>1.07</sub>Si<sub>0.15</sub> coating deposited at a substrate bias of  $-100$  V and a Si-target power of 50 W (region II in Figure 5, under an indent): (a) lattice image and SAD pattern, (b) FFT image marked in (a) (solid circles: possible complete dislocations; dashed circles: possible partial dislocations).

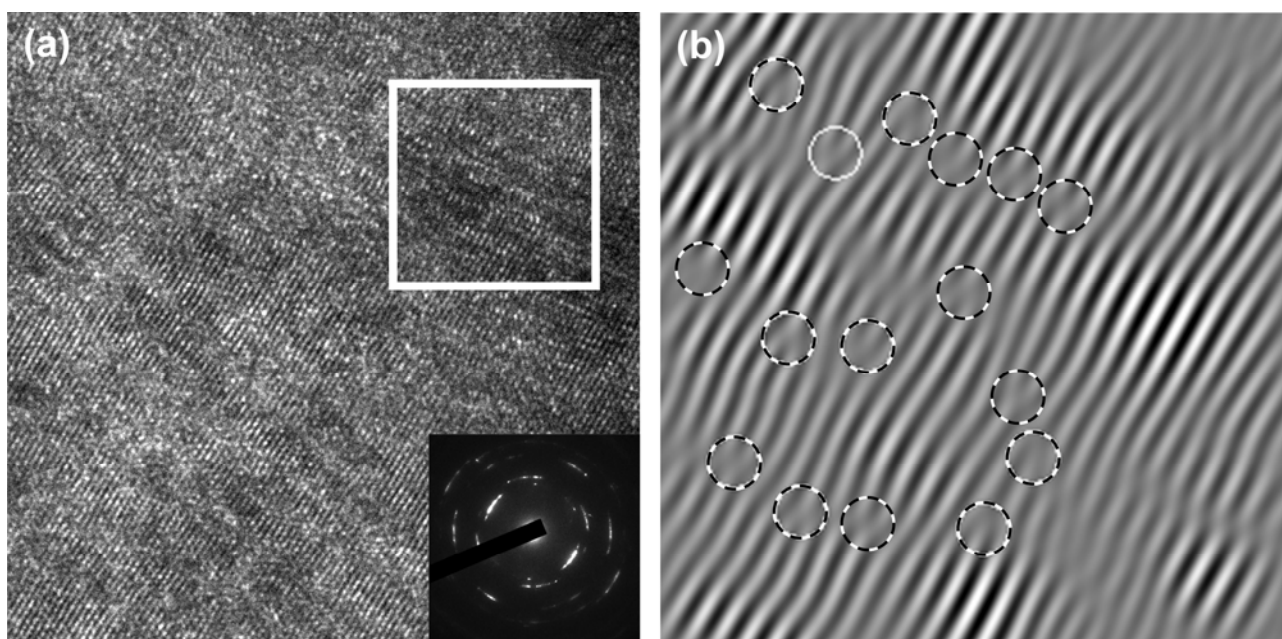
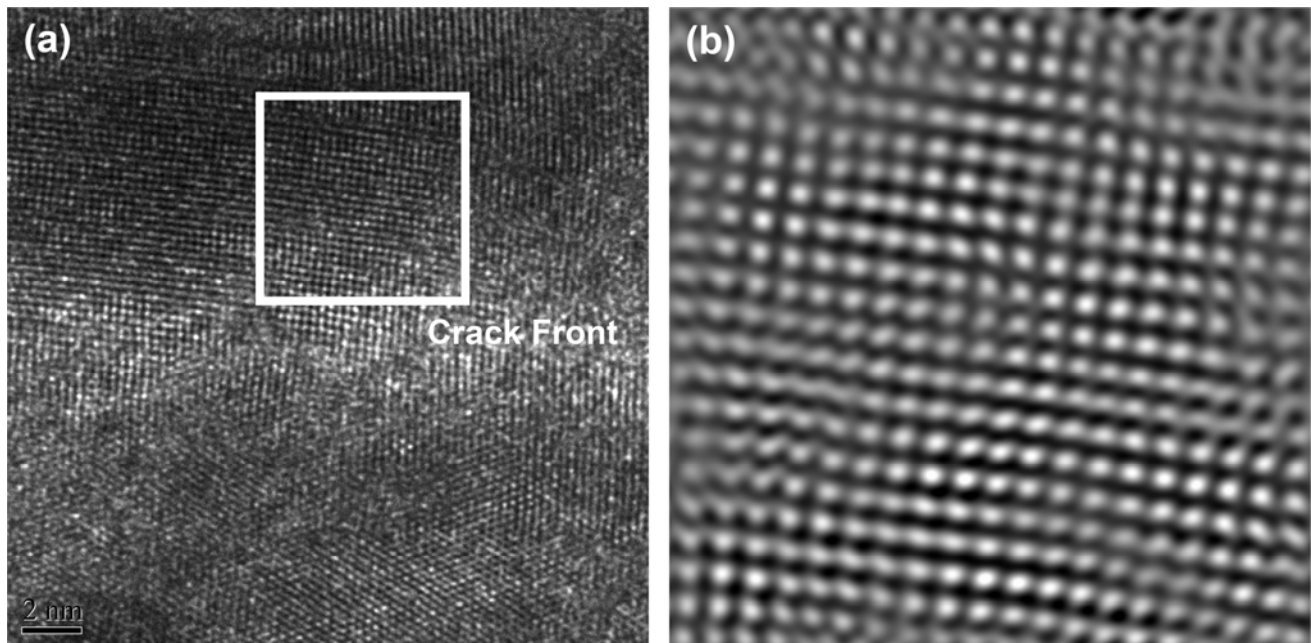


**Figure 8.** HRTEM analyses of stress-released HEAN<sub>1.07</sub>Si<sub>0.15</sub> coating deposited at a substrate bias of  $-100$  V and a Si-target power of 50 W (region III in Figure 5, around a crack): (a) lattice image, (b) FFT image marked in (a).



#### 4. Conclusions

Multi-component HEAN<sub>x</sub>Si<sub>y</sub> high-entropy coatings with a simple fcc solid-solution structure were prepared by co-sputtering of AlCrTaTiCr alloy and Si targets in an Ar/N<sub>2</sub> mixed atmosphere with the application of different substrate biases and Si-target powers. Upon increasing the substrate bias to  $-100$  V and Si-target power to 50 W, the coatings transformed from a large columnar structure with a [111] preferred orientation to a nanocomposite structure composed of surrounding amorphous SiN-based layers at the boundaries of dispersed ultrafine nitride grains. The hardness, H/E ratio and H<sup>3</sup>/E<sup>2</sup> ratio were highly enhanced to 30.2 GPa, 0.12 and 0.41 GPa, respectively, revealing a high resistance to wear and plastic deformation, because of grain refinements, film densification, the nanocomposite structure, the inhibition of nitride grain growth by the surrounding amorphous SiN-based layers, and the severe lattice distortions of the coatings. Severe lattice distortions and consequent high strain energy caused by the incorporations of different-size atoms suppressed the activities of complete dislocations under stresses, but facilitated the formation of stacking faults and partial dislocations which dominated the deformation behaviors of the multi-component HEAN<sub>x</sub>Si<sub>y</sub> high-entropy coatings.

#### Acknowledgments

The authors gratefully acknowledge financial supports for this research by the National Science Council, Taiwan, under Grant No. NSC-100-2628-E-005-006-MY3, and in part by the Ministry of Education, Taiwan, under the ATU plan.

## Conflicts of Interest

The authors declare no conflict of interest.

## References

1. Pierson, H.O. *Handbook of Refractory Carbides & Nitrides: Properties, Characteristics, Processing and Applications*; Noyes Publications: Westwood, NJ, USA, 1996.
2. Fouvry, S.; Wendler, B.; Liskiewicz, T.; Dudek, M.; Kolodziejczyk, L. Fretting wear analysis of TiC/VC multilayered hard coatings: Experiments and modelling approaches. *Wear* **2004**, *257*, 641–653.
3. Balaceanu, M.; Braic, M.; Braic, V.; Pavelescu, G. Properties of arc plasma deposited TiCN/ZrCN superlattice coatings. *Surf. Coat. Tech.* **2005**, *200*, 1084–1087.
4. Hyakutake, H.; Imada, Y.; Honda, F.; Nakajima, K. Mechanical properties of TiN-TiC mixed crystal films. *J. Phys. Condens. Matter* **1998**, *10*, 111–121.
5. Manghnani, M.H.; Tkachev, S.N.; Zinin, P.V.; Glorieux, C.; Karvankova, P.; Veprek, S. Elastic properties of nc-TiN/a-SiN and nc-TiN/a-BN nanocomposite films by surface brillouin scattering. *J. Appl. Phys.* **2005**, *97*, 054308.
6. Veprek, S.; Zhang, R.; Veprek-Heijman, M.; Sheng, S.; Argon, A. Superhard nanocomposites: Origin of hardness enhancement, properties and applications. *Surf. Coat. Tech.* **2010**, *204*, 1898–1906.
7. Kim, S.; Kim, B.; Kim, G.; Lee, S.; Lee, B. Evaluation of the high temperature characteristics of the CrZrN coatings. *Surf. Coat. Tech.* **2008**, *202*, 5521–5525.
8. Silva, E.; Rebelo de Figueiredo, M.; Franz, R.; Escobar Galindo, R.; Palacio, C.; Espinosa, A.; Calderon V, S.; Mitterer, C.; Carvalho, S. Structure-property relations in ZrCN coatings for tribological applications. *Surf. Coat. Tech.* **2010**, *205*, 2134–2141.
9. Pengfei, H.; Bailing, J. Study on tribological property of CrCN coating based on magnetron sputtering plating technique. *Vacuum* **2011**, *85*, 994–998.
10. Chen, R.; Tu, J.; Liu, D.; Mai, Y.; Gu, C. Microstructure, mechanical and tribological properties of TiCN nanocomposite films deposited by dc magnetron sputtering. *Surf. Coat. Tech.* **2011**, *205*, 5228–5234.
11. Guo, Y.; Ma, S.; Xu, K. Effects of carbon content and annealing temperature on the microstructure and hardness of super hard Ti-Si-C-N nanocomposite coatings prepared by pulsed dc pcvd. *Surf. Coat. Tech.* **2007**, *201*, 5240–5243.
12. Zhang, X.; Jiang, J.; Yuqiao, Z.; Lin, J.; Wang, F.; Moore, J.J. Effect of carbon on TiAlCN coatings deposited by reactive magnetron sputtering. *Surf. Coat. Tech.* **2008**, *203*, 594–597.
13. Pogrebniak, A.; Shpak, A.; Kirik, G.; Erdybaeva, N.; Il'yashenko, M.; Dem'yanenko, A.; Kunitskii, Y.A.; Kaverina, A.S.; Baidak, V.; Makhmudov, N. Multilayered nano-microcomposite Ti-Al-N/TiN/Al<sub>2</sub>O<sub>3</sub> coatings. Their structure and properties. *Acta Phys. Pol. A* **2011**, *120*, 94–99.
14. Yeh, J.W.; Chen, S.K.; Lin, S.J.; Gan, J.Y.; Chin, T.S.; Shun, T.T.; Tsau, C.H.; Chang, S.Y. Nanostructured high-entropy alloys with multiple principal elements: Novel alloy design concepts and outcomes. *Adv. Eng. Mater.* **2004**, *6*, 299–303.

15. Tong, C.J.; Chen, M.R.; Yeh, J.W.; Lin, S.J.; Chen, S.K.; Shun, T.T.; Chang, S.Y. Mechanical performance of the Al<sub>x</sub>CoCrCuFeNi high-entropy alloy system with multiprincipal elements. *Metall. Mater. Trans. A* **2005**, *36*, 1263–1271.
16. Chuang, M.H.; Tsai, M.H.; Wang, W.R.; Lin, S.J.; Yeh, J.W. Microstructure and wear behavior of Al<sub>x</sub>Co<sub>1.5</sub>CrFeNi<sub>1.5</sub>Ti<sub>y</sub> high-entropy alloys. *Acta Mater.* **2011**, *59*, 6308–6317.
17. Lai, C.H.; Lin, S.J.; Yeh, J.W.; Chang, S.Y. Preparation and characterization of AlCrTaTiZr multi-element nitride coatings. *Surf. Coat. Tech.* **2006**, *201*, 3275–3280.
18. Huang, P.K.; Yeh, J.W. Effects of nitrogen content on structure and mechanical properties of multi-element (AlCrNbSiTiV)N coating. *Surf. Coat. Tech.* **2009**, *203*, 1891–1896.
19. Chang, S.Y.; Lin, S.Y.; Huang, Y.C.; Wu, C.L. Mechanical properties, deformation behaviors and interface adhesion of (AlCrTaTiTr)N<sub>x</sub> multi-component coatings. *Surf. Coat. Tech.* **2010**, *204*, 3307–3314.
20. Cheng, K.H.; Tsai, C.W.; Lin, S.J.; Yeh, J.W. Effects of silicon content on the structure and mechanical properties of (AlCrTaTiZr)-Si<sub>x</sub>-N coatings by reactive rf magnetron sputtering. *J. Phys. Appl. Phys.* **2011**, *44*, 205405.
21. Lin, S.Y.; Chang, S.Y.; Huang, Y.C.; Shieu, F.S.; Yeh, J.W. Mechanical performance and nanoindenting deformation of (AlCrTaTiZr)NC<sub>y</sub> multi-component coatings co-sputtered with bias. *Surf. Coat. Tech.* **2012**, *206*, 5096–5102.
22. Barshilia, H.C.; Deepthi, B.; Arun Prabhu, A.; Rajam, K. Superhard nanocomposite coatings of TiN/Si<sub>3</sub>N<sub>4</sub> prepared by reactive direct current unbalanced magnetron sputtering. *Surf. Coat. Tech.* **2006**, *201*, 329–337.
23. Veprek, S.; Reiprich, S. A concept for the design of novel superhard coatings. *Thin Solid Films* **1995**, *268*, 64–71.
24. Diserens, M.; Patscheider, J.; Levy, F. Mechanical properties and oxidation resistance of nanocomposite TiN-SiN<sub>x</sub> physical-vapor-deposited thin films. *Surf. Coat. Tech.* **1999**, *120*, 158–165.
25. Flink, A.; Larsson, T.; Sjöln, J.; Karlsson, L.; Hultman, L. Influence of si on the microstructure of arc evaporated (Ti, Si) N thin films; evidence for cubic solid solutions and their thermal stability. *Surf. Coat. Tech.* **2005**, *200*, 1535–1542.
26. Veprek, S.; Veprek-Heijman, M.G.; Karvankova, P.; Prochazka, J. Different approaches to superhard coatings and nanocomposites. *Thin Solid Films* **2005**, *476*, 1–29.
27. Carvalho, S.; Rebouta, L.; Cavaleiro, A.; Rocha, L.; Gomes, J.; Alves, E. Microstructure and mechanical properties of nanocomposite (Ti, Si, Al) N coatings. *Thin Solid Films* **2001**, *398*, 391–396.
28. Li, Z.; Mori, M.; Miyake, S.; Kumagai, M.; Saito, H.; Muramatsu, Y. Structure and properties of Ti-Si-N films prepared by icp assisted magnetron sputtering. *Surf. Coat. Tech.* **2005**, *193*, 345–349.
29. Pilloud, D.; Pierson, J.; Marques, A.; Cavaleiro, A. Structural changes in Zr-Si-N films vs. their silicon content. *Surf. Coat. Tech.* **2004**, *180*, 352–356.
30. Chang, C.L.; Huang, C.S. Effect of bias voltage on microstructure, mechanical and wear properties of Al-Si-N coatings deposited by cathodic arc evaporation. *Thin Solid Films* **2011**, *519*, 4923–4927.
31. Park, I.W.; Kang, D.S.; Moore, J.J.; Kwon, S.C.; Rha, J.J.; Kim, K.H. Microstructures, mechanical properties, and tribological behaviors of Cr-Al-N, Cr-Si-N, and Cr-Al-Si-N coatings by a hybrid coating system. *Surf. Coat. Tech.* **2007**, *201*, 5223–5227.

32. Huang, Y.C.; Chang, S.Y.; Chang, C.H. Effect of residual stresses on mechanical properties and interface adhesion strength of SiN thin films. *Thin Solid Films* **2009**, *517*, 4857–4861.
33. Chen, J.; Bull, S. On the factors affecting the critical indenter penetration for measurement of coating hardness. *Vacuum* **2009**, *83*, 911–920.
34. Sandu, C.; Sanjinés, R.; Benkahoul, M.; Medjani, F.; Lévy, F. Formation of composite ternary nitride thin films by magnetron sputtering co-deposition. *Surf. Coat. Tech.* **2006**, *201*, 4083–4089.
35. Cullity, B.D.; Stock, S.R. *Elements of X-Ray Diffraction*; Prentice Hall: Upper Saddle River, NJ, USA, 2001.
36. Mayrhofer, P.H.; Mitterer, C.; Hultman, L.; Clemens, H. Microstructural design of hard coatings. *Progr. Mater. Sci.* **2006**, *51*, 1032–1114.
37. Zhang, R.; Veprek, S. Phase stabilities and spinodal decomposition in the  $\text{Cr}_{1-x}\text{Al}_x\text{N}$  system studied by ab initio lda and thermodynamic modeling: Comparison with the  $\text{Ti}_{1-x}\text{Al}_x\text{N}$  and  $\text{TiN/Si}_3\text{N}_4$  systems. *Acta Mater.* **2007**, *55*, 4615–4624.
38. Lai, C.H.; Lin, S.J.; Yeh, J.W.; Davison, A. Effect of substrate bias on the structure and properties of multi-element (AlCrTaTiZr)N coatings. *J. Phys. Appl. Phys.* **2006**, *39*, 4628.
39. Huang, P.K.; Yeh, J.W. Effects of substrate bias on structure and mechanical properties of (AlCrNbSiTiV)N coatings. *J. Phys. Appl. Phys.* **2009**, *42*, 115401.
40. Musil, J.; Novak, P.; Cerstvy, R.; Soukup, Z. Tribological and mechanical properties of nanocrystalline-TiC/a-C nanocomposite thin films. *J. Vac. Sci. Tech.* **2010**, *28*, 244–249.
41. Shaginyan, L.R.; Han, J.G.; Britun, N.V. Effect of the surface temperature on formation of low-temperature phase in magnetron-sputtered chromium films. *Jpn. J. Appl. Phys.* **2005**, *44*, 3200–3204.
42. Williams, D.B.; Carter, C.B. *The Transmission Electron Microscope*; Springer: New York, NY, USA, 2009.
43. Abbaschian, R.; Abbaschian, L.; Hill, R.E.R. *Physical Metallurgy Principles*; Cengage Learning: Stamford, CT, USA, 2009.

© 2013 by the authors; licensee MDPI, Basel, Switzerland. This article is an open access article distributed under the terms and conditions of the Creative Commons Attribution license (<http://creativecommons.org/licenses/by/3.0/>).